

**Anharmonicity in elastic constants and extended x-ray-absorption fine structure cumulants**

Toshihiko Yokoyama\* and Suwilai Chaveanghong†

*Department of Materials Molecular Science, Institute for Molecular Science, Myodaiji-cho, Okazaki, 444-8585, Japan*

(Received 28 December 2018; published 21 March 2019)

We have investigated temperature dependence of the elastic constants and higher-order EXAFS (extended x-ray-absorption fine structure) cumulant moments, both of which originate from vibrational anharmonicity. We focus our attention on how the third- or fourth-order anharmonicity contributes to these physical quantities. Although it may be believed that the fourth-order anharmonicity should dominantly contribute to the fourth-order EXAFS cumulant through the first-order quantum statistical perturbation theory, it is consequently found that the experimental fourth-order EXAFS cumulant observed in fcc Ni, Cu, and stainless steel 316 are described mainly by the third-order anharmonicity through the second-order perturbation. In case of the elastic constants, such a situation is more prominent, and the contribution of the fourth-order anharmonicity is negligibly small for the estimation of temperature dependence of the elastic constants. We have also observed significant lattice strains on Cr and Mo in stainless steel 316 through the Fe, Ni, Cr, and Mo K-edge EXAFS measurements: a compressive lattice strain on Cr associated with larger thermal fluctuations and a more significant compressive lattice strain on Mo without enhanced thermal fluctuation. Such a characteristic dissimilarity may be caused by the differences in the atomic weights and the cohesive energies between Cr and Mo. Moreover, we have performed path-integral effective classical potential and classical Monte-Carlo simulations to describe the bulk moduli of the Invar and Elinvar alloys that show noticeable anomalies due to the so-called Invar effect. Appropriate temperature dependence of the bulk moduli is successfully obtained for the Invar, Elinvar, and stainless steel 304 and 316 alloys as well as elemental fcc Cu and Ni metals.

DOI: [10.1103/PhysRevMaterials.3.033607](https://doi.org/10.1103/PhysRevMaterials.3.033607)**I. INTRODUCTION**

It is well known that thermal expansion of matters originates from vibrational anharmonicity of the system and that when the interatomic potential is Taylor expanded around the equilibrium distance, the third-order anharmonicity dominantly contributes to thermal expansion. Since the interatomic potential is usually steeper at a shorter distance side than at a longer distance side, the third-order expansion coefficient of the interatomic potential is negative. This leads to elongation of the interatomic distance with a temperature rise, which is regarded as thermal expansion. The remark that the origin of thermal expansion is ascribed to the third-order anharmonicity is quite natural, and many investigations have so far been performed in detail using macroscopic dilatometry, x-ray diffraction, and extended x-ray-absorption fine structure (EXAFS) spectroscopy. EXAFS can determine the cumulant moments of the radial distribution function around x-ray absorbing atoms with high accuracy and allows one to discuss local thermal expansion in detail, which may often differ from lattice (macroscopic) thermal expansion.

On the other hand, temperature variation of elastic constants such as bulk moduli and Young moduli is also caused by vibrational anharmonicity. The elastic constant corresponds to the second-order differential coefficient of the interatomic potential around the equilibrium distance, and within the

harmonic approximation it should be constant upon temperature variation, as in the case of the interatomic distance. It is however well known even in our daily lives that most materials become softer with a temperature rise, implying a decrease in the elastic constant with temperature. Although it is in general supposed that temperature dependence of the elastic constant can be ascribed to both the odd- and even-order anharmonic contributions [1–6], only very few investigations concerning temperature dependent elastic constants of real materials have been conducted based on experimental or computational methods. In terms of EXAFS, the third-order cumulant moment  $C_3$  is given as  $C_3 = \langle (r - R)^3 \rangle$ , where  $\langle \rangle$  denotes the thermal average,  $r$  is the instantaneous interatomic distance between the x-ray absorbing and photoelectron scattering neighboring atoms, and  $R$  is the thermally averaged distance  $R = \langle r \rangle$ . The EXAFS third-order cumulant  $C_3$ , which is sometimes called the mean cubic relative displacement, describes asymmetry of the radial distribution function around the x-ray absorbing atom and has been extensively investigated [7–28]. The relation between the third-order force constant and thermal expansion is well understood both theoretically and experimentally. In contrast, the relationship between the fourth-order cumulant and the fourth-order force constant has poorly been investigated especially for experiments of real material systems, and to the best of our knowledge there has been no direct report concerning temperature dependent elastic constants by EXAFS.

In the present work, we have investigated temperature dependence of the force constants, in which the odd (third) and even (fourth) order constants are distinguished by the EXAFS

\*yokoyama@ims.ac.jp

†suwilai.materialscience@gmail.com

analysis and are comparatively discussed about their contributions. Here, we have obtained the average interatomic distance  $R$ , the second-order cumulant  $C_2 = \langle (r - R)^2 \rangle$  (mean square relative displacement), the third-order cumulant  $C_3$ , and the fourth-order cumulant  $C_4 = \langle (r - R)^4 \rangle - 3C_2^2$ , and have analyzed the contributions of the anharmonic force constants to the cumulants. Especially, the relation between the fourth-order cumulant and the fourth-order force constant has been analyzed in detail. As sample specimens, we employed well known materials as elemental fcc Cu and Ni metals, and also SUS316L (AISI316L stainless steel,  $\text{Fe}_{67}\text{Cr}_{18}\text{Ni}_{12}\text{Mo}_2\text{Mn}_1$ ) with various metal atoms that can be studied by Fe, Ni, Cr, and Mo K-edge EXAFS. Element specific effective local force constants are characteristic in EXAFS and we can recognize some differences in the force constants as well as the interatomic distances among the elements studied, although the SUS316 forms a simple fcc lattice in average. Rather surprisingly, it is found that the third-order anharmonicity dominates the fourth-order EXAFS cumulant and temperature dependence of the effective force constant, while the fourth-order force constant is of no importance to describe especially temperature dependence of the elastic constants. In the SUS316 alloy, the effective potential around Cr is found to be softer (the effective force constant is smaller) than those around other metal elements.

Moreover, in the present investigation, we have also examined possible lattice strains in the SUS316 alloy. In our previous EXAFS study [29] on the Elinvar ( $\text{Ni Span C}$ ,  $\text{Fe}_{49.66}\text{Ni}_{42.38}\text{Cr}_{5.49}\text{Ti}_{2.47}$ ) and SUS304 (AISI304 stainless steel,  $\text{Fe}_{71.98}\text{Ni}_{9.07}\text{Cr}_{18.09}\text{Mn}_{0.86}$ ) alloys, it was found that the lattice strains are concentrated around Cr. Here, we have examined a possible lattice strain on Mo. In case of SUS304, the local structure around Cr is slightly compressed, and it will be interesting to identify whether the local structure around Mo, which is the  $4d$  transition metal element with a much larger atomic radius, is compressed or expanded. As a result of SUS316, it is elucidated that the lattice strains around both Cr and Mo are observed, while almost no strains are detected around Ni. The compression around Cr is similar to that in SUS304, and the one around Mo is more prominent and the metallic radius of Mo in SUS316 is even smaller than a usual metallic radius of bcc Mo, although the absolute value of the interatomic distance around  $4d$  metal Mo is naturally larger than the other  $3d$  transition metal atoms.

Finally, we have performed computational simulations concerning the bulk moduli of the Invar ( $\text{Fe}_{64}\text{Ni}_{36}$ ), Elinvar, SUS304, SUS316 alloys, together with fcc Ni and Cu, by means of the path-integral effective classical potential (PIECP) [20–23,30–36] and classical Monte-Carlo (MC) methods. The Invar alloy is a well known alloy that shows almost negligible thermal expansion over a wide temperature range and an anomaly of increase in the elastic constant with a temperature rise [30–32,37–40]. See Figs. S1 and S2 in the Supplemental Material [41] for temperature dependence, respectively, of the interatomic distances and the Young moduli of the Invar, Elinvar, and SUS304 alloys. The Invar alloy has technologically been applied to many industrial materials such as precision equipments and recently has been employed as a core of electric power lines. The Elinvar alloy exhibits almost no temperature dependence of the elastic constants around

room temperature with a smaller thermal expansion than normal metals. Temperature dependence of the bulk moduli is found to be semiquantitatively in good agreement with the experimental observations. There have been presented only very few works concerning the quantum mechanical simulations of temperature dependent elastic constants [42,43], although the general fundamental quantum mechanical theories have been well established [1–6]. We have also successfully discussed the vibrational quantum effect (zero-point vibrational fluctuation) concerning these alloys as well as fcc Ni and Cu.

The present paper is organized as follows. In Sec. II, experimental and theoretical methods are described in detail. Section III deals with the results and discussion, in which the relationship between the higher-order force constants and cumulant moments will at first be discussed, followed by discussion about the lattice strains on Cr and Mo atoms in SUS316, and eventually providing the simulated results on the bulk moduli of the alloy materials. In Sec. IV, concluding remarks of the present investigation are summarized.

## II. EXPERIMENT AND THEORY

### A. EXAFS

The Cr, Fe, Ni, and Mo K-edge EXAFS spectra of commercially available SUS316L alloy foils (Nilaco Corp., Japan) with thicknesses of  $10\ \mu\text{m}$  for Cr, Fe, and Ni K edge and  $200\ \mu\text{m}$  for Mo K edge were recorded at Beamlines 9C [44] and 12C [45] of Photon Factory (the electron storage ring energy of 2.5 GeV and the ring current of 450–300 mA) in High Energy Accelerator Research Organization (KEK-PF) with the transmission mode using a Si(111) double crystal monochromator. The concentrations of the metals contained were verified semiquantitatively in advance using x-ray fluorescence spectrometer in Instrument Center of Institute for Molecular Science. For the Cr and Fe K-edge EXAFS measurements, the monochromator crystals were detuned by 30% to eliminate the third-order harmonics, while for the Ni and Mo K-edge measurements the detuning process was not conducted. In Cr, Fe, and Ni K-edge EXAFS, ionization chambers filled with 30%  $\text{N}_2$  in He (17 cm in length) and 100%  $\text{N}_2$  (31 cm) were used to measure the incident and transmitted x-ray intensities, respectively, while in Mo K-edge EXAFS, those filled with 50% Ar and 50%  $\text{N}_2$  (17 cm) and 100% Ar (31 cm  $\times$  2) were employed for the incident and transmitted x rays, respectively. The samples were cooled down using a He gas-circulating refrigerator and the measurement temperature range was 20–300 K. The Cr and Ni K-edge EXAFS measurements were terminated, respectively, at the Mn and Cu K edge because of the presence of small amounts of Mn and Cu in the SUS316 alloy, while the Fe and Mo K-edge EXAFS were successfully recorded over sufficiently wide energy ranges.

The EXAFS oscillation functions  $k^3\chi(k)$  ( $k$  the photoelectron wave number) were obtained based on the standard procedures as the pre-edge baseline and the post-edge background subtractions and the subsequent normalization with atomic absorption coefficients. The  $k^3\chi(k)$  functions were subsequently Fourier transformed, Fourier filtered for the peaks of interest, and were finally curve fitted in  $k$  space. In the present study, the first- and third-nearest neighbor (NN) shells were quantitatively analyzed. The Fe, Ni, Cr, and Mo K-edge

EXAFS  $k^3\chi(k)$  functions and their Fourier transforms are depicted in Figs. S3–S6, respectively, and the  $k$  and  $R$  spaces employed are summarized in Table S1 in the Supplemental Material [41].

The single-shell EXAFS formula employed is given as

$$\chi(k) = \frac{S_0^2 N F(k)}{kR^2} \exp\left[-2C_2 k^2 + \frac{2}{3}C_4 k^4\right] \times \sin\left[2kR + \phi(k) - \frac{4}{3}C_3 k^3\right], \quad (1)$$

where  $N$  is the coordination number,  $S_0^2$  the intrinsic reduction factor due to the many-electron effect,  $F(k)$  the backscattering amplitude including the inelastic scattering loss factor, and  $\phi(k)$  the total phase shift between the x-ray absorbing and photoelectron scattering atoms.

For the curve-fitting analysis to obtain the structural parameters, theoretical standards were at first calculated using FEFF8.4 [46]. Here, we assumed randomly distributed clusters with the perfect fcc lattice constant of 3.57129 Å (the number of the fcc unit lattices of  $4^3$  and the total number of atoms of  $4 \times 4^3 = 256$ ), where the composition ratio of the SUS316 alloy was assumed to be  $\text{Fe}_{68}\text{Ni}_{12}\text{Cr}_{18}\text{Mo}_2$  (Mn neglected). Ten random alloy clusters were evaluated and the average EXAFS spectra were obtained as consequent theoretical standards. Although static lattice strains are actually expected in these alloys, the FEFF simulations were conducted with the assumption that all the atoms are distributed at ideal lattice positions. Note here that the neighboring atoms around the x-ray absorbing atom are assumed not to be distinguished because of only small differences of the backscattering amplitudes among Fe, Ni, and Cr and of only a small amount of Mo in SUS316, and therefore the resultant values obtained experimentally are regarded as the average one for each x-ray absorbing atom.

The curve-fitting analysis of the experimental EXAFS spectra at the lowest temperature was subsequently performed using the FEFF standards obtained above. Here, the parameters fitted were  $S_0^2$ ,  $R$ ,  $\Delta E_0$  (edge energy shift), and  $C_2$  (fixed at  $N = 12$  for the first-NN shells and  $N = 24$  for the third-NN shells,  $C_3 = 0$  and  $C_4 = 0$ ). The fitting results are summarized in Table S2 in the Supplemental Material [41]. Finally, the curve-fitting analysis of all the EXAFS spectra were carried out using the lowest temperature data as empirical standards, with the assumption that  $S_0^2$ ,  $N$ , and  $\Delta E_0$  are identical to the ones at the lowest temperature, while  $R$ ,  $C_2$ ,  $C_3$ , and  $C_4$  are fitting variables for the first-NN shells, and  $R$  and  $C_2$  are fitting variables for the third-NN shells. Note here that higher-order cumulants in the third-NN shells are known to be neglected with high accuracy because of the absence of the chemical bonds that induces anharmonicity [20], as in the central limit theorem that random distribution without correlation approaches Gaussian distribution.

## B. PIECP MC simulations

In order to investigate temperature dependence of bulk moduli of Invar, Elinvar, SUS304, and SUS316 alloys, we have performed PIECP MC simulations [33–36] under a constant number of particles, pressure, and temperature (NPT) condition. The interatomic potentials of Fe, Ni, Cr,

and Mo are based on the empirical embedded-atom method (EAM) [47–49]. The numerical parameters of nonmagnetic (NM, or antiferromagnetic or low spin) Fe, Ni, Cr, and Mo employed were the modified EAM potentials [49]. In Fe, the energy difference between the ferromagnetic (FM, or high spin) and NM states were employed as in the previous works [29–31]. For comparison, the MC simulations based on the classical thermodynamics were also carried out.

The compositions of the alloys in the simulations were assumed to be  $\text{Fe}_{64}\text{Ni}_{36}$  for Invar,  $\text{Fe}_{52.2}\text{Ni}_{42.4}\text{Cr}_{5.4}$  for Elinvar (Ti neglected),  $\text{Fe}_{72}\text{Ni}_9\text{Cr}_{19}$  for SUS304 (Mn neglected), and  $\text{Fe}_{68}\text{Ni}_{12}\text{Cr}_{18}\text{Mo}_2$  for SUS316 (Mn neglected). The total number of atoms was 500 ( $5^3$  fcc cubic unit cells), and the distributions of Fe, Ni, Cr, and Mo were chosen randomly. In a similar manner to the FEFF evaluations, ten types of the superlattices were simulated and the results were averaged to provide consequent physical quantities. The MC simulations were performed based on the conventional Metropolis method, where 100 000 MC steps were calculated with 500 times trials of the atom movement and one trial of the lattice constant variation in each MC step. In the calculations of thermodynamical quantities, the results before the system reaches sufficient equilibrium ( $\sim 20$  000 MC steps) were excluded. The temperatures considered in the present simulations were in the range of 10–400 K.

Although the quantum effect in the elastic constant has been long known, computational simulations based on the quantum mechanical method as the path integral theory have seldom been performed [42,43], and to the best of our knowledge no investigations using the PIECP theory have been conducted. Moreover, only very limited works using the EAM potentials were carried out even within the classical dynamics simulation; an example is found for fcc Ni [50]. In order to verify the reliability of the present computational simulations, we have also conducted the PIECP and classical MC simulations for elemental fcc Ni and Cu metals. In the calculations of bulk moduli, five pressures were chosen as  $P = 0, \pm 2, \text{ and } \pm 4$  (GPa) and the bulk moduli were estimated from the variation of the equilibrium lattice constants.

One additional hypothesis in the present PIECP simulations should be noted here. The PIECP theory is based on the periodic lattice dynamics to correct the vibrational quantum fluctuations and to estimate effective classical potentials and is strictly not applicable to the present random alloy systems as Invar, Elinvar, SUS304, or SUS316. These alloys however exhibit clear fcc structure and the lattice periodicity can approximately be assumed. We have estimated the variance of the interatomic potential around all the atoms employed. The standard deviations estimated in SUS304 are 1.1% in the equilibrium distance, 2.8% in the potential depth, and 18% in the second derivative of the potential at the equilibrium distance. The phonon dispersion curves may exhibit some fluctuations based on these deviations concerning the interatomic potentials. In the present simulations, however, the magnitude of the quantum corrections is found to be quite small concerning the bulk modulus in SUS304, which is only 0.4% at 10 K and 0.2% at 300 K. The consequent deviations due to inaccurate periodicity of random alloys should thus be less than 0.1% even at 10 K, which is negligibly small to discuss temperature dependence of the bulk moduli.

### III. RESULTS AND DISCUSSION

#### A. Relationship between higher-order EXAFS cumulants and anharmonic interatomic potential

Let us first recall the relationship between higher-order EXAFS cumulants and a simple two-body anharmonic interatomic potential by referring to the previous works [13,14,23]. The two-body anharmonic interatomic potential  $V(r)$  ( $r$  is the interatomic distance) is given in a Taylor expanded form as

$$V(r) = \frac{1}{2}\kappa_0(r - R_0)^2 - \kappa_3(r - R_0)^3 + \kappa_4(r - R_0)^4, \quad (2)$$

where the first term is the harmonic term with harmonic force constant  $\kappa_0$ , and the second and third terms can be regarded as the perturbed third- and fourth-order anharmonic terms with anharmonic force constants  $\kappa_3$  and  $\kappa_4$ , respectively.  $R_0$  is the distance at the potential minimum. These constants as  $\kappa_0$ ,  $\kappa_3$ ,  $\kappa_4$ , and  $R_0$  are assumed to be temperature independent.

Using the quantum statistical second-order perturbation theory, the thermally averaged physical quantities as  $R$ ,  $C_2$ ,  $C_3$ , and  $C_4$  are evaluated, which can be obtained experimentally by the EXAFS measurements. The interatomic distance  $R$  and the third-order cumulant  $C_3$  are given within the first-order perturbation theory as

$$R \simeq R_0 + \frac{6\kappa_3\sigma_0^4}{\hbar\omega} \frac{1+z}{1-z} \quad (3)$$

and

$$C_3 \simeq C_3^{(1)} = \frac{\kappa_3\sigma_0^6}{\hbar\omega} \frac{4(z^2 + 10z + 1)}{(1-z)^2}, \quad (4)$$

where  $z = \exp[-\hbar\omega/k_B T]$  ( $k_B$  the Boltzmann constant,  $T$  the temperature,  $\hbar = h/2\pi$ ,  $h$  the Planck constant,  $\omega = \sqrt{\kappa_0/m}$ , and  $m$  the reduced mass of the oscillator) and  $\sigma_0^2 = \hbar/2m\omega$  (zero-point vibrational amplitude). Note that the thermal expansion given in the second term in Eq. (3) and the third-order cumulant are both proportional to the third-order force constant  $\kappa_3$ .

On the other hand, the second-order cumulant  $C_2$  and the fourth-order cumulant  $C_4$  are given in the second-order perturbation as

$$C_2 \simeq C_2^{(0)} + C_2^{(1)} + C_2^{(2)}, \quad (5)$$

$$C_2^{(0)} = \sigma_0^2 \frac{1+z}{1-z}, \quad (6)$$

$$C_2^{(1)} = -\frac{\kappa_4\sigma_0^6}{\hbar\omega} \frac{12(1+z)^2}{(1-z)^2} - \frac{\kappa_4\sigma_0^6}{k_B T} \frac{24z(1+z)}{(1-z)^3}, \quad (7)$$

$$C_2^{(2)} = \frac{\kappa_3^2\sigma_0^8}{(\hbar\omega)^2} \frac{4(13z^2 + 58z + 13)}{(1-z)^2} + \frac{\kappa_3^2\sigma_0^8}{(\hbar\omega)(k_B T)} \frac{120z(1+z)}{(1-z)^3} \quad (8)$$

and

$$C_4 \simeq C_4^{(1)} + C_4^{(2)}, \quad (9)$$

$$C_4^{(1)} = -\frac{\kappa_4\sigma_0^8}{\hbar\omega} \frac{12(z^3 + 9z^2 + 9z + 1)}{(1-z)^3} - \frac{\kappa_4\sigma_0^8}{k_B T} \frac{144z^2}{(1-z)^4}, \quad (10)$$

$$C_4^{(2)} = \frac{\kappa_3^2\sigma_0^{10}}{(\hbar\omega)^2} \frac{12(5z^3 + 109z^2 + 109z + 5)}{(1-z)^3} + \frac{\kappa_3^2\sigma_0^{10}}{(\hbar\omega)(k_B T)} \frac{720z^2}{(1-z)^4}, \quad (11)$$

where  $C_2^{(0)}$  is the harmonic contribution,  $C_2^{(1)}$  and  $C_4^{(1)}$  are the first-order perturbation terms that are proportional to the fourth-order force constant  $\kappa_4$ , and  $C_2^{(2)}$  and  $C_4^{(2)}$  are the second-order perturbation terms proportional to the square of the third-order force constant  $\kappa_3$ . Note here that in  $C_2$  and  $C_4$ , the first- and second-order perturbation terms are in the same order; although the second-order perturbation terms apparently exhibit higher order in  $\sigma_0^2$ , the factor  $\hbar\omega$  is present in the denominator in the second-order perturbation terms [Eqs. (8) and (11)] and the two terms are resultantly in the same order. The first-order terms  $C_2^{(1)}$  and  $C_4^{(1)}$  are both negative with positive  $\kappa_4$ , while the second-order terms  $C_2^{(2)}$  and  $C_4^{(2)}$  are positive. It is also noted that all the anharmonic terms are finite even at  $T = 0$ , this implying for example that the average interatomic distance  $R$  at  $T = 0$  is longer than the potential minimum  $R_0$ .

The classical limits ( $\hbar \rightarrow 0$ ) of the above formulas can easily be calculated as

$$R_{cl} \simeq R_0 + \frac{3\kappa_3}{\kappa_0^2} k_B T, \quad (12)$$

$$C_{3,cl} \simeq \frac{6\kappa_3}{\kappa_0^3} (k_B T)^2, \quad (13)$$

$$C_{2,cl} \simeq \frac{k_B T}{\kappa_0} + 12 \left( -\frac{\kappa_4}{\kappa_0^3} + \frac{3\kappa_3^2}{\kappa_0^4} \right) (k_B T)^2, \quad (14)$$

and

$$C_{4,cl} \simeq 12 \left( -\frac{2\kappa_4}{\kappa_0^4} + \frac{9\kappa_3^2}{\kappa_0^5} \right) (k_B T)^3. \quad (15)$$

These classical expressions clearly show that at high temperature, thermal expansion [the second term in Eq. (12)] and harmonic term of  $C_2$  [the first term in Eq. (14)] are proportional to temperature  $T$ , while the third- and fourth-order cumulants  $C_3$  and  $C_4$  are proportional to the squared and cubed temperature  $T^2$  and  $T^3$ , respectively.

Figures 1(a)–1(d) shows the EXAFS cumulants of fcc Cu fitted with the above anharmonic oscillator models. Since the absolute values of the experimentally obtained structure parameters may contain some inaccurate contribution, we will discuss mainly about temperature dependence that is more accurate and more important in the present purpose. The absolute values of the experimental data in Figs. 1(a)–1(d) were thus shifted to match the calculated ones at the lowest temperature. The amount of the shift in  $C_2$  is  $-0.0046 \times 10^{-2} \text{ \AA}$ , and the origin of the discrepancy is ascribed mainly to inaccuracy in the backscattering amplitude derived from the theoretical standard and partly to inaccuracy in the simple two-body model interatomic potential. The amounts of the shifts in  $C_3$  and  $C_4$  are negligibly small but are inherently expected because the experimental results correspond to the difference from the lowest-temperature data.

In the second-order cumulants  $C_2$  in Fig. 1(a), the quantum mechanical results agree quite well with the experiments

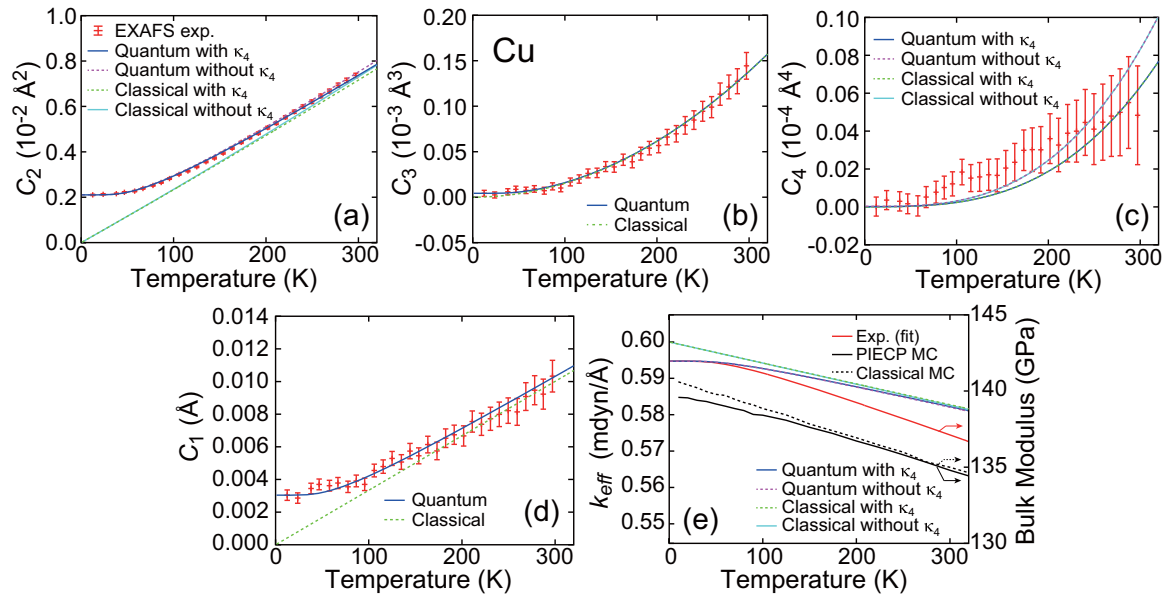


FIG. 1. Results of the Cu K-edge EXAFS analysis of fcc Cu. Experimental EXAFS results of (a)  $C_2$ , (b)  $C_3$ , (c)  $C_4$ , and (d)  $C_1 = R - R_0$  are given as red symbols with error bars. The fitting results using the simple anharmonic oscillator models are depicted as blue solid (quantum including  $\kappa_4$ ), purple dotted (quantum neglecting  $\kappa_4$ ), green dotted (classical including  $\kappa_4$ ), and light blue solid (classical neglecting  $\kappa_4$ ) lines in (a) and (c). (e) Temperature dependence of effective force constants  $k_{\text{eff}}$  using the left axis. The bulk moduli discussed later are also plotted for comparison as red solid (experimental), black solid (PIECP), and black dotted (classical MC) lines using the right axis. For details, see the text.

especially for a downwardly convex curvature at low temperature, while the classical results show almost linear dependence with large deviations from the experiment at low temperature. The calculated results including the fourth-order force constant  $\kappa_4$  (blue solid line) are slightly smaller than those neglecting  $\kappa_4$  (purple dotted line), because the first-order perturbation contribution in Eq. (7) is negative. In the third-order cumulant  $C_3$  in Fig. 1(b), the classical result shows very slight deviation from the quantum mechanical ones at low temperature. The fourth-order cumulants  $C_4$  give noticeable difference between the  $\kappa_4$ -including and  $\kappa_4$ -neglecting results; the  $\kappa_4$ -including one is smaller than the  $\kappa_4$ -neglecting one due to a negative contribution of the first-order perturbation term in Eq. (10) as in the case of  $C_2$  in Fig. 1(a). It is important to note here that concerning the contribution to the fourth-order EXAFS cumulant  $C_4$ , the second-order perturbation of the third-order anharmonicity is more significant than the first-order perturbation of the fourth-order anharmonicity. Experimentally obtained  $C_4$  is clearly positive and increases with a temperature rise, which cannot be described by the first-order perturbation of the fourth-order anharmonicity but should be attributed to the second-order perturbation of the third-order anharmonicity.

Figure 1(e) shows temperature dependence of the effective force constants  $k_{\text{eff}}$  of fcc Cu, which are given as the second derivatives of the two-body potential function at the thermally averaged interatomic distance. The classical results exhibit a nearly linear function down to  $T = 0$ , while the quantum results give an upwardly convex function at low temperature due to the zero-point vibrational quantum effect. The most important finding in Fig. 1(e) is that the fourth-order force constant  $\kappa_4$  exhibits almost no contribution to temperature dependence of the effective force constant. This is easily

found out when one compares the  $\kappa_4$ -including result (blue solid line) with the  $\kappa_4$ -neglecting one (purple dotted line). As in the above discussion for the fourth-order EXAFS cumulant  $C_4$ , this consequence again implies that temperature dependence of the effective force constant is ascribed almost exclusively to the second-order perturbation of the third-order anharmonicity, not to the first-order perturbation of the fourth-order anharmonicity.

In Fig. 1(e), the results of the bulk moduli given by the following PIECP (black solid line) and classical (black dotted line) MC simulations are also depicted, which are basically proportional to the effective force constants  $k_{\text{eff}}$ . The red solid line corresponds to the experimental data. Here the vibrational quantum effect is again observed; the experimental and quantum mechanical PIECP results show upwardly convex functions, while the classical result exhibits a linear function. The bulk modulus  $B$  and the temperature coefficient  $\alpha = (1/B)(dB/dT)$  at  $T = 300$  K are estimated to be  $B = 135$  (GPa) and  $\alpha = -1.43 \times 10^{-4}$  (1/K) by the PIECP MC simulations, which yield excellent agreements with the experimental ones of  $B = 137$  (GPa) and  $\alpha = -1.58 \times 10^{-4}$  (1/K) [51]. Similar results concerning fcc Ni were obtained in this work, and the corresponding plots are shown in Fig. S7 in the Supplemental Material [41]. The PIECP simulations of fcc Ni give  $B = 177$  (GPa) and  $\alpha = -9.56 \times 10^{-5}$  (1/K) at  $T = 300$  K, which are similarly in good agreement with the experimental ones of  $B = 184$  (GPa) and  $\alpha = -9.53 \times 10^{-5}$  (1/K) [52].

Let us subsequently discuss the results of SUS316. Since it is already found in the above fcc Cu (and Ni) analysis that contribution of the fourth-order anharmonicity to the bulk modulus is not significant, the fourth-order force constant  $\kappa_4$  was not considered in the analysis of SUS316. We will here

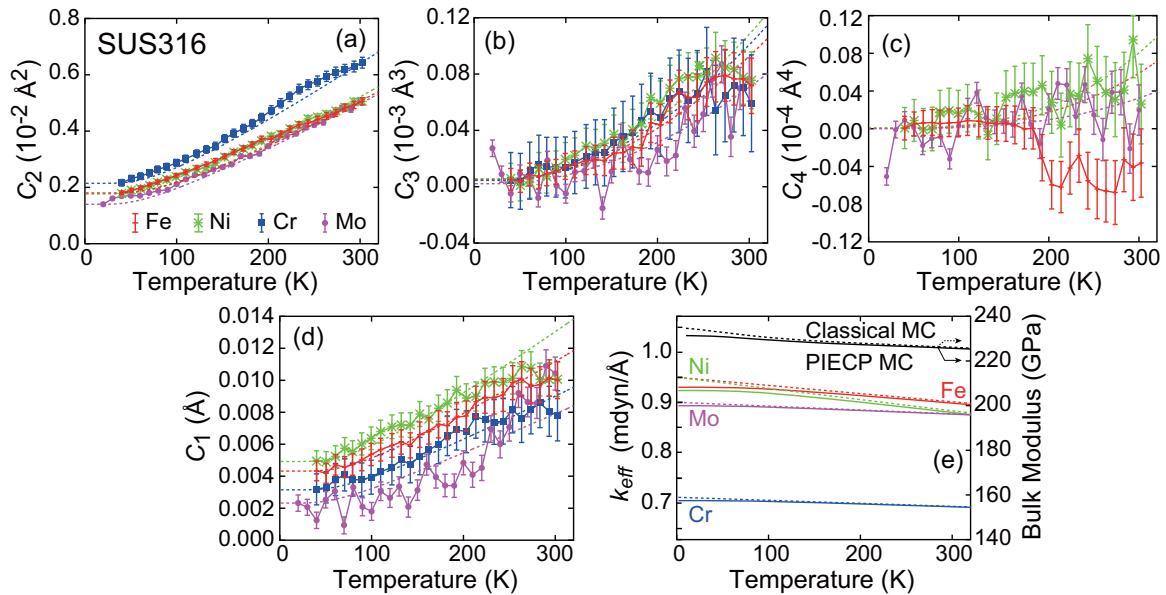


FIG. 2. Results of the Fe, Ni, Cr, and Mo K-edge EXAFS analysis of SUS316. Experimental EXAFS results of (a)  $C_2$ , (b)  $C_3$ , (c)  $C_4$ , and (d)  $C_1 = R - R_0$  are given as solid lines with error bars (Fe: red; Ni: green; Cr: blue; Mo: purple), while the fitting results using the simple quantum mechanical anharmonic oscillator models neglecting  $\kappa_4$  are depicted as dashed lines. (e) Temperature dependence of effective force constants  $k_{\text{eff}}$  using the left axis. The bulk moduli discussed later are also plotted for comparison as black solid (PIECP) and black dotted (classical MC) lines using the right axis.

mainly consider the differences in the metallic elements in the SUS316 alloy. Similarly to the case in Fig. 1, the absolute values of the experimental data in Figs. 2(a)–2(d) were shifted to match the calculated ones at the lowest temperature. The amounts of the shifts in  $C_2$  are much larger than that in the fcc Cu case:  $0.193 \times 10^{-2} \text{ \AA}$  for Fe,  $0.114 \times 10^{-2} \text{ \AA}$  for Ni,  $0.152 \times 10^{-2} \text{ \AA}$  for Cr, and  $0.083 \times 10^{-2} \text{ \AA}$  for Mo. The origin of the shifts is attributed dominantly to the static disorder in the alloy sample and partly to inaccuracies in the theoretical FEFF standard and the simple two-body interatomic potential. Note that the shifts in  $C_3$  and  $C_4$  are negligibly small, although the obtained  $C_3$  and  $C_4$  correspond to thermal ones and do not include static disorder.

Figure 2 depicts the EXAFS cumulants and the effective force constants  $k_{\text{eff}}$  of SUS316, and the numerical results are summarized in Table I, together with the results of fcc Cu and Ni. In Fig. 2(a), temperature dependence of  $C_2$  in Cr (blue) is clearly larger than the other elements, indicating a smaller harmonic force constant  $\kappa_0$  in Cr. The EXAFS cumulants

$C_2$ ,  $C_3$ , and  $C_4$  seem to be slightly smaller in Mo, probably because of a heavier atomic weight and a larger cohesive energy than the other elements. Thermal expansion given as  $C_1$  in Fig. 2(d) is found to be consistently estimated from the third-order cumulants  $C_3$  in Fig. 2(b). As a consequence, Cr is found to be thermally more fluctuated than the other elements. On the contrary, a heavier atom Mo interestingly shows smaller thermal fluctuations. The thermal fluctuations will be discussed in the next subsection that deals with lattice strains. In Fig. 2(e), the calculated effective force constants  $k_{\text{eff}}$  are shown, together with the bulk moduli obtained by the PIECP and classical MC simulations. The effective force constant  $k_{\text{eff}}$  estimated from the Cr results yields a much smaller value than the other ones. In the PIECP and classical MC results of the bulk moduli, although the vibrational quantum effect can also be seen at low temperature, the classical results exhibit a slight downwardly convex function (not a linear function), indicating complexity in the alloy dynamics and a possible presence of temperature dependent structural disorder.

TABLE I. Harmonic and anharmonic force constants  $\kappa_0$ ,  $\kappa_3$ , and  $\kappa_4$  and the equilibrium distance  $R_0$  (potential minimum) determined by the EXAFS analysis of fcc Cu, Ni, and SUS316. The numbers in parentheses after the last digit implies the fitting errors. The fourth-order force constant  $\kappa_4$  was neglected in the SUS316 analysis.

sample	central atom	$m$ [g/mol]	$R_0$ [Å]	$\kappa_0$ [mdyn/Å]	$\kappa_3$ [mdyn/Å <sup>2</sup> ]	$\kappa_4$ [mdyn/Å <sup>3</sup> ]
fcc Ni	Ni	58.69	2.486(1)	0.90(1)	0.35(2)	0.10(4)
fcc Cu	Cu	63.55	2.542(1)	0.60(1)	0.29(2)	0.15(4)
SUS316	Fe	55.85	2.527(1)	0.95(1)	0.77(3)	
	Ni	58.69	2.527(2)	0.95(2)	0.90(4)	
	Cr	52.00	2.497(2)	0.71(2)	0.35(3)	
	Mo	95.94	2.581(2)	0.90(2)	0.50(3)	

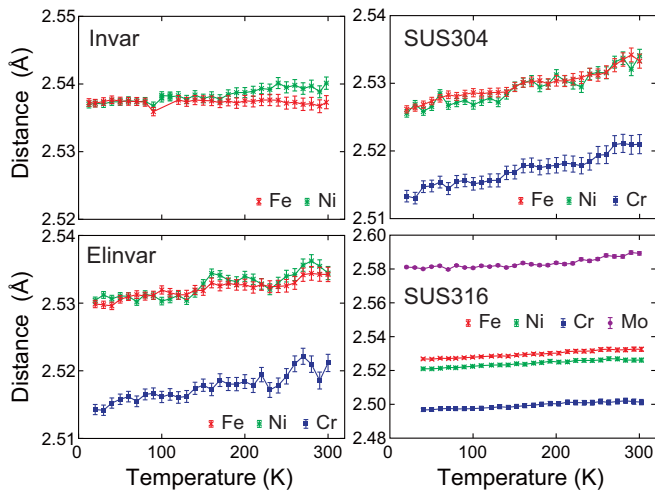


FIG. 3. The first-NN interatomic distances of Invar [30,31], Elinvar [29], SUS304 [29], and SUS316 (present work) alloys determined by Fe, Ni, Cr, and Mo K-edge EXAFS (points with error bars). Note that the coordinated atoms (scatterer) are not elementarily distinguished, while the central atoms (x-ray absorber) are clearly distinguished.

### B. Interatomic distances and lattice strains in SUS316

We will next consider the interatomic distances in SUS316 in order to see element dependent lattice strains. Figure 3 shows temperature dependence of the first-NN interatomic distances around the x-ray absorbing atoms in the Invar [30,31], Elinvar [29], SUS304 [29], and SUS316. Those of the third-NN distances are depicted in Fig. S8 in Supplemental Material [41]. The Invar alloy exhibits almost no thermal expansion around Fe and small expansion around Ni [ $-0.03 \times 10^{-5}$  (Å/K) for Fe and  $1.02 \times 10^{-5}$  (Å/K) for Ni] [30,31]. In the case of the Elinvar alloy, thermal expansion around Fe is noticeably smaller than those of Ni and Cr [ $1.33 \times 10^{-5}$  (Å/K) for Fe,  $2.17 \times 10^{-5}$  (Å/K) for Ni, and  $2.32 \times 10^{-5}$  (Å/K) for Cr], while in SUS304, all the thermal expansions around Fe, Ni, and Cr are essentially similar and quite normal [ $2.39 \times 10^{-5}$  (Å/K) for Fe,  $2.40 \times 10^{-5}$  (Å/K) for Ni, and  $2.85 \times 10^{-5}$  (Å/K) for Cr] [29]. Although the vertical scale in SUS316 differs from the other ones, local thermal expansion around Fe, Ni, Cr, and Mo are not extraordinary showing a normal thermal expansion behavior [ $2.50 \times 10^{-5}$  (Å/K) for Fe,  $2.32 \times 10^{-5}$  (Å/K) for Ni,  $2.16 \times 10^{-5}$  (Å/K) for Cr, and  $3.19 \times 10^{-5}$  (Å/K) for Mo].

We will here focus our attention on the absolute value of the interatomic distance around each x-ray absorbing atom. Assuming that the alloys show completely random distributions of metal elements and that the radius of each metal atom is uniquely given irrespective of the neighboring elements, the metallic radii of all the elements in the alloys can be estimated by using the EXAFS results. In SUS304 and SUS316, the Fe atomic radii is estimated to be 1.264 and 1.266 Å, respectively, which are slightly larger than that of bcc Fe (1.239 Å) and are quite reasonable because of larger coordination numbers in fcc alloys. The Ni atomic radii are given as 1.268 Å for SUS304 and 1.265 Å for SUS316, again slightly larger than that of fcc Ni (1.243 Å). It is consequently remarked that Fe

and Ni atoms have essentially the same interatomic distances for the first-NN shells and form alloy structures with high commensurability.

In contrast, the environment around Cr significantly differs from those around Fe and Ni. As shown in Fig. 3, the first-NN interatomic distances around Cr in SUS304 are shortened by  $\sim 0.015$  Å compared with those around Fe and Ni, and in the present SUS316, this trend is more prominently observed. The Cr atomic radii are estimated to be 1.251 and 1.235 Å for SUS304 and SUS316, respectively, which are similar to that of bcc Cr (1.246 Å) or even shorter. The fact that in the fcc lattice with larger first-NN coordination numbers yields similar or shorter interatomic distances around Cr implies the presence of large compressive lattice strain around Cr. On the other hand, the Mo atomic radius in SUS316 is given as 1.319 Å, being shorter by as much as 0.04 Å than that of bcc Mo (1.358 Å), indicating more significant compressive lattice strain in Mo atoms with inherently larger atomic radii. It is interesting to note that the thermal fluctuation around Cr is larger than those on the other metals as mentioned in the previous subsection, which may reasonably coincide with a large compressive lattice strain on Cr, while the thermal fluctuation around Mo is smaller with a more significant compressive lattice strain, probably due to a heavier atomic weight and a larger cohesive energy. It can be concluded that although the Invar, Elinvar, SUS304, and SUS316 alloys are recognized to form fcc lattices with completely random atomic distributions, the real interatomic distances are considerably dependent on the elements.

### C. Temperature dependent bulk moduli of the Invar, Elinvar, SUS304, and SUS316 alloys

At the last of the present investigation, we will discuss the bulk moduli of the Invar, Elinvar, SUS304, and SUS316 alloys calculated by the PIECP and classical MC methods. First of all, the Invar effect [37,38] is shortly recalled using the present potential parameters. Figure 4 and Table II give average interatomic potentials around Fe in Invar, Elinvar, and SUS316 at  $T = 0$ . The calculations were performed by varying only the lattice constant keeping a perfect fcc lattice. In the Invar alloy at  $T = 0$ , all the Fe atoms are in the stable ferromagnetic (FM) high-spin state with a longer equilibrium distance and a smaller bulk modulus (see Table II for numerical values), and the unstable nonmagnetic (NM) low-spin state with a shorter interatomic distance and a larger bulk modulus locates 0.034 eV above the FM state. With an increase in temperature, the population of the NM state gradually increases. The average interatomic distance is thus shortened, and as a result normal thermal expansion due to anharmonic vibration is compensated, leading to negligible overall thermal expansion in the Invar alloy. This is the Invar effect proposed by Weiss [38] as a simple two-state model.

On the other hand, in the SUS316 alloy, the NM state is more stable than the FM state, and the energy difference is as much as 0.124 eV, leading to insignificant anti-Invar effect even at high temperature. The stability of the NM state in Fe can be ascribed to the presence of Cr (and Mo). As the  $d$  electron density of the neighboring atoms increases, the Fe atom is likely to be nonmagnetic. In the present EAM

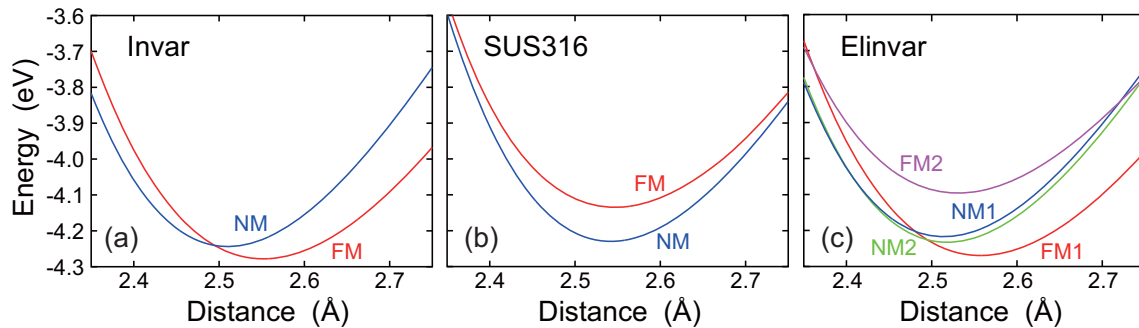


FIG. 4. Potential diagrams around Fe atoms in (a) Invar, (b) SUS316, and (c) Elinvar alloys. FM and NM denote the ferromagnetically coupled high-spin and nonmagnetic low-spin Fe, respectively.

simulations, the  $d$  electron energy is exactly described as a function of  $d$  electron density. Although the number of  $d$  electrons in Cr is smaller than that of Ni, the Cr  $3d$  orbitals are much more extended than those of Ni, yielding a larger  $d$  electron density at the neighboring Fe site and resultant stabilization of the NM Fe state. It can be remarked that the Fe atoms surrounded by many Ni atoms are likely to be ferromagnetic, while those surrounded by many Cr atoms to be nonmagnetic.

In case of the Elinvar alloy, the situation is more complicated. There exist two stable Fe states (FM1 and NM2) at  $T = 0$ ; the one (Fe1) favors the FM state, while the other (Fe2) does the NM state, depending on the kinds of neighboring atoms. With a temperature rise, some Fe1 atoms are thermally excited from the FM1 to NM1 state (the energy difference of 0.053 eV). Since the NM1 state exhibits a smaller interatomic distance and a larger bulk modulus, the Elinvar alloy shows the partial Invar effect associated with a small thermal expansion and a nearly constant bulk modulus. On the other hand, the NM2 state in Fe2 is hardly thermally excited to the FM2 state because of a larger energy difference of 0.134 eV. This is the explanation of the Elinvar effect based on the simple two-state Weiss model [38].

Figure 5 depicts the bulk moduli and the FM ratios of Fe in the Invar, Elinvar, SUS304, and SUS316 alloys, simulated by the PIECP and classical MC methods. The calculated bulk moduli of fcc Ni and Cu are plotted again for comparison. As mentioned above, the FM ratio of Fe decreases noticeably with a temperature rise in the Invar alloy, and the Elinvar alloy exhibit smaller but meaningful reduction of the FM ratio

TABLE II. Equilibrium distance  $R_{eq}$ , potential depth  $D$ , and bulk modulus  $B$  of ferromagnetic high-spin (FM) and nonmagnetic low-spin (NM) Fe states evaluated from the potential curves in Fig. 4.

alloy	state	$R_{eq}$ [Å]	$D$ [eV]	$B$ [GPa]
Invar	FM	2.553	4.278	147
	NM	2.512	4.244	182
SUS316	FM	2.549	4.135	143
	NM	2.544	4.230	177
Elinvar	FM1	2.559	4.270	143
	NM1	2.516	4.233	173
	NM2	2.520	4.217	175
	FM2	2.533	4.096	131

in a similar manner. On the other hand, the stainless steel alloys give small increase in the FM Fe population with a temperature rise, indicating occurrence of thermal excitations to unstable FM states to some extent. Correspondingly, the bulk modulus of the Invar alloy is at first reduced at a low temperature region (0–100 K), where the FM Fe population does not decrease so much, and is subsequently enhanced at a high temperature region (200–400 K) due to the Invar effect. In the Elinvar alloy, a similar explanation can be made, and the resultant bulk modulus exhibits temperature invariance at the range of 200–400 K. The present PIECP and classical simulations have successfully provided reasonable descriptions

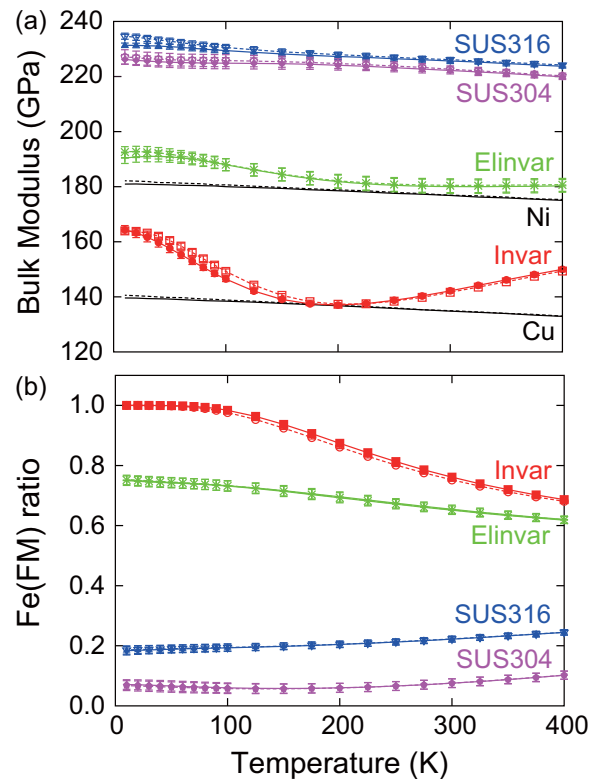


FIG. 5. (a) Bulk moduli and (b) Fe(FM) ratios in Invar (red), Elinvar (green), SUS304 (blue), and SUS316 (purple) alloys simulated by the PIECP (solid) and classical (dashed) MC calculations. The results of the bulk moduli of fcc Cu and Ni are also shown as black solid and dashed lines.

of the Invar and Elinvar effects at least semiquantitatively. Although the vibrational quantum effect in these alloy systems is not significant as seen in Fig. 5, the convergence features toward  $T \rightarrow 0$  are described well in the PIECP simulations, which is demonstrated to be useful for the understanding of low temperature thermodynamical properties of matters.

#### IV. CONCLUSIONS

The purposes of the present investigation are threefold, and the most important issue is to understand how the third-order or fourth-order anharmonicity contributes to temperature dependence of the elastic constants as bulk moduli and also the fourth-order EXAFS cumulant  $C_4$ . It seems to have been believed that the fourth-order anharmonicity characterized by the fourth-order force constant  $\kappa_4$  should dominantly contribute to the fourth-order EXAFS cumulant  $C_4$  through the first-order quantum statistical perturbation theory with the harmonic oscillator as a nonperturbed system. Since the first-order perturbation term originating from the fourth-order anharmonicity is negative and the second-order perturbation from the third-order anharmonicity is positive, it is rather easily distinguishable which term exhibits dominant contribution by analyzing the EXAFS experimentally. It is found that the experimental  $C_4$  values are positive and increases with a temperature rise in fcc Cu and Ni and the calculated contributions are significantly larger in the second-order perturbation from the third-order anharmonicity. Somewhat surprisingly, this implies that the third-order anharmonicity contributes more strongly to the fourth-order EXAFS cumulant. In the case of effective force constants or bulk moduli, such a situation is more prominent, and the contribution of the third-order anharmonicity is dominant, allowing one to neglect the fourth-order anharmonicity for the estimation of temperature dependence of the elastic constants.

The second purpose in this work is a possible lattice strain in SUS316. In the previous work [29], it was found that the lattice strain in SUS304 is concentrated on Cr. We have found here that the compressive lattice strain on Cr is more significant in SUS316, associated with larger thermal fluctuations on Cr. The compressive lattice strain is observed more prominently on Mo, where the Mo atomic radius in fcc SUS316 is even shorter than that in elemental bcc Mo with a smaller first-NN coordination number. It is interesting that the thermal fluctuation around Mo is smaller in contrast to the Cr case, probably because Mo is much heavier and has a much larger cohesive energy than the other  $3d$  metals. The third purpose in the present work is to simulate the bulk moduli of the Invar and Elinvar alloys that show anomaly due to the Invar effect. We have carried out the quantum mechanical PIECP and classical MC simulations for these alloys, together with the metals with normal behaviors concerning temperature dependence of the bulk modulus and thermal expansion. We have successfully obtained appropriate temperature dependence of the bulk moduli of all the metals investigated semiquantitatively.

#### ACKNOWLEDGMENTS

We would like to thank beamline staffs in KEK-PF for their technical helps in the EXAFS measurements. We are grateful for the partial financial support by JSPS (Japan Society for the Promotion of Science) KAKENHI Grant No. JP15H02173. The EXAFS measurements at Photon Factory have been performed under the approval of Photon Factory Program Advisory Committee (PF-PAC proposal No. 2017G034). The staffs in Instrument Center of Institute for Molecular Science are also acknowledged for the x-ray fluorescence spectroscopic measurements.

- 
- [1] M. Born, *J. Chem. Phys.* **7**, 591 (1939).
  - [2] M. Born and K. Huang, *Dynamical Theory of Crystal Lattices* (Clarendon, Oxford, 1954).
  - [3] E. A. Stern, *Phys. Rev.* **111**, 786 (1958).
  - [4] C. Feldman, M. L. Klein, and G. K. Horton, *Phys. Rev.* **184**, 910 (1969).
  - [5] J. A. Garber and A. V. Granato, *Phys. Rev. B* **11**, 3990 (1975).
  - [6] J. A. Garber and A. V. Granato, *Phys. Rev. B* **11**, 3998 (1975).
  - [7] P. Eisenberger and G. S. Brown, *Solid State Commun.* **29**, 481 (1979).
  - [8] G. Bunker, *Nucl. Instrum. Methods* **207**, 437 (1983).
  - [9] J. M. Tranquada and R. Ingalls, *Phys. Rev. B* **28**, 3520 (1983).
  - [10] E. D. Crozier, J. J. Rehr, and R. Ingalls, *X-ray Absorption: Principles, Applications of EXAFS, SEXAFS and XANES*, edited by D. C. Koningsberger and R. Prins (Wiley, New York, 1988), Chap. 9.
  - [11] T. Yokoyama, T. Satsukawa, and T. Ohta, *Jpn. J. Appl. Phys.* **28**, 1905 (1989).
  - [12] L. Wenzel, D. Arvanitis, H. Rabus, T. Lederer, K. Baberschke, and G. Comelli, *Phys. Rev. Lett.* **64**, 1765 (1990).
  - [13] H. Rabus, Ph.D. thesis, Department of Physics, Freie Universität Berlin, 1991.
  - [14] A. I. Frenkel and J. J. Rehr, *Phys. Rev. B* **48**, 585 (1993).
  - [15] T. Fujikawa and T. Miyanaga, *J. Phys. Soc. Jpn.* **62**, 4108 (1993).
  - [16] T. Yokoyama, K. Kobayashi, T. Ohta, and A. Ugawa, *Phys. Rev. B* **53**, 6111 (1996).
  - [17] A. Di Cicco, A. Filipponi, J. P. Itié, and A. Polian, *Phys. Rev. B* **54**, 9086 (1996).
  - [18] T. Yokoyama, Y. Yonamoto, T. Ohta, and A. Ugawa, *Phys. Rev. B* **54**, 6921 (1996).
  - [19] H. Wende, D. Arvanitis, M. Tischer, R. Chauvistre, H. Henneken, F. May, and K. Baberschke, *Phys. Rev. B* **54**, 5920 (1996).
  - [20] T. Yokoyama, T. Ohta, and H. Sato, *Phys. Rev. B* **55**, 11320 (1997).
  - [21] T. Fujikawa, T. Miyanaga, and T. Suzuki, *J. Phys. Soc. Jpn.* **66**, 2897 (1997).
  - [22] T. Yokoyama, *Phys. Rev. B* **57**, 3423 (1998).
  - [23] T. Yokoyama, *J. Synchrotron Radiat.* **6**, 323 (1999).

- [24] G. Dalba, P. Fornasini, R. Grisenti, and J. Purans, *Phys. Rev. Lett.* **82**, 4240 (1999).
- [25] A. Filippini, A. Di Cicco, and S. De Panfilis, *Phys. Rev. Lett.* **83**, 560 (1999).
- [26] S. a Beccara, G. Dalba, P. Fornasini, R. Grisenti, A. Sanson, and F. Rocca, *Phys. Rev. Lett.* **89**, 025503 (2002).
- [27] A. Di Cicco, A. Trapananti, S. Faggioni, and A. Filippini, *Phys. Rev. Lett.* **91**, 135505 (2003).
- [28] P. Fornasini, S. a Beccara, G. Dalba, R. Grisenti, A. Sanson, M. Vaccari, and F. Rocca, *Phys. Rev. B* **70**, 174301 (2004).
- [29] T. Yokoyama, A. Koide, and Y. Uemura, *Phys. Rev. Mater.* **2**, 023601 (2018).
- [30] T. Yokoyama and K. Eguchi, *Phys. Rev. Lett.* **107**, 065901 (2011).
- [31] T. Yokoyama, *e-J. Surf. Sci. Nanotech.* **10**, 486 (2012).
- [32] T. Yokoyama and K. Eguchi, *Phys. Rev. Lett.* **110**, 075901 (2013).
- [33] A. Cuccoli, V. Tognetti, A. A. Maradudin, A. R. McGurn, and R. Vaia, *Phys. Rev. B* **46**, 8839 (1992).
- [34] A. Cuccoli, V. Tognetti, A. A. Maradudin, A. R. McGurn, and R. Vaia, *Phys. Rev. B* **48**, 7015 (1993).
- [35] A. Cuccoli, R. Giachetti, V. Tognetti, R. Vaia, and P. Verrucchi, *J. Phys.: Condens. Matter* **7**, 7891 (1995).
- [36] A. Cuccoli, V. Tognetti, R. Vaia, and P. Verrucchi, *Phys. Rev. Lett.* **77**, 3439 (1996).
- [37] C. E. Guillaume, *C. R. Hebd. Séances Acad. Sci.* **125**, 235 (1897).
- [38] R. J. Weiss, *Proc. Phys. Soc. London A* **82**, 281 (1963).
- [39] Y. S. Touloukian, R. E. Kirby, R. E. Taylor, and P. D. Desai, *Thermophysical Properties of Matter Vol. 12, Thermal Expansion Metallic Elements and Alloys* (Plenum, New York, 1975).
- [40] W. S. McCain and R. Maringer, *Mechanical and Physical Properties of Invar and invar-Type Alloys* (Battell Memorial Institute, Defense Metals Information Center, Columbus, Ohio, 1965).
- [41] See Supplemental Material at <http://link.aps.org/supplemental/10.1103/PhysRevMaterials.3.033607> for supplemental figures and tables.
- [42] R. Ramírez, C. P. Herrero, and E. R. Hernández, *Phys. Rev. B* **73**, 245202 (2006).
- [43] R. Martoňák, W. Paul, and K. Binder, *Phys. Rev. E* **57**, 2425 (1998).
- [44] <http://pfxafs.kek.jp/beamline/bl9c/>
- [45] <http://pfxafs.kek.jp/beamline/bl12c/>
- [46] A. L. Ankudinov, A. I. Nesvizhskii, and J. J. Rehr, *Phys. Rev. B* **67**, 115120 (2003).
- [47] M. S. Daw and M. I. Baskes, *Phys. Rev. B* **29**, 6443 (1984).
- [48] S. M. Foiles, *Phys. Rev. B* **32**, 3409 (1985).
- [49] M. I. Baskes, *Phys. Rev. B* **46**, 2727 (1992).
- [50] M. Karimiy, G. Stapayy, T. Kaplanz, and M. Mostollerz, *Modell. Simul. Mater. Sci. Eng.* **5**, 337 (1997).
- [51] Y. P. Varshni, *Phys. Rev. B* **2**, 3952 (1970).
- [52] G. A. Alers, J. R. Neighbours, and H. Sato, *J. Phys. Chem. Solids* **13**, 40 (1960).